



# Photocatalytic Properties of Bismuth Oxyfluoride Thin Films Deposited by Reactive Magnetron Sputtering in Ar/O<sub>2</sub>/CF<sub>4</sub> Atmosphere

Sara Ibrahim, Liana Minasyan, Pierre Bonnet, Guillaume Monier, Eric Tomasella, Thierry Sauvage, Mireille Richard-Plouet, Maryline Le Granvalet, Audrey Bonduelle, Celine Pagis, et al.

## ► To cite this version:

Sara Ibrahim, Liana Minasyan, Pierre Bonnet, Guillaume Monier, Eric Tomasella, et al.. Photocatalytic Properties of Bismuth Oxyfluoride Thin Films Deposited by Reactive Magnetron Sputtering in Ar/O<sub>2</sub>/CF<sub>4</sub> Atmosphere. 2023. hal-04037069

**HAL Id: hal-04037069**

**<https://hal.science/hal-04037069>**

Preprint submitted on 20 Mar 2023

**HAL** is a multi-disciplinary open access archive for the deposit and dissemination of scientific research documents, whether they are published or not. The documents may come from teaching and research institutions in France or abroad, or from public or private research centers.

L'archive ouverte pluridisciplinaire **HAL**, est destinée au dépôt et à la diffusion de documents scientifiques de niveau recherche, publiés ou non, émanant des établissements d'enseignement et de recherche français ou étrangers, des laboratoires publics ou privés.

## Photocatalytic Properties of Bismuth Oxyfluoride Thin Films Deposited by Reactive Magnetron Sputtering in Ar/O<sub>2</sub>/CF<sub>4</sub> Atmosphere

Sara Ibrahim <sup>a</sup>, Liana Minasyan <sup>a</sup>, Pierre Bonnet <sup>a</sup>, Guillaume Monier <sup>b</sup>, Eric Tomasella<sup>a</sup>, Thierry Sauvage <sup>c</sup>, Mireille Richard-Plouet<sup>d</sup>, Maryline Le Granvalet <sup>d</sup>, Audrey Bonduelle <sup>e</sup>, Celine Pagis <sup>e</sup>, Angelique Bousquet <sup>a\*</sup>

<sup>a</sup> Université Clermont Auvergne, Institut de Chimie de Clermont-Ferrand (ICCF), 24 Avenue Blaise Pascal, 63178 Aubière, France

<sup>b</sup> Université Clermont Auvergne, Institut Pascal (IP), 4 Avenue Blaise Pascal, 63178 Aubière, France

<sup>c</sup> Conditions Extrêmes et Matériaux sous Haute Température et sous Irradiation (CEMHTI), 45071 Orléans, France

<sup>d</sup> Institut des Matériaux de Nantes Jean Rouxel, 2 rue de la Houssinière, 44322 Nantes, France

<sup>e</sup> IFP ENERGIES NOUVELLES, Rond-Point de l'Echangeur de Solaize, 69360 Solaize, France

### Abstract

Bismuth oxyfluoride films were successfully deposited by reactive magnetron sputtering in different Ar/O<sub>2</sub>/CF<sub>4</sub> gas mixtures. Films deposited with a reactive gas ratio ( $R_f$ ), which is the O<sub>2</sub> to (O<sub>2</sub> + CF<sub>4</sub>) flow rates ratio, ranging between 0 and 0.5 consist of two phases, BiO<sub>0.5</sub>F<sub>2</sub> and metallic bismuth (Bi<sup>0</sup>); whereas for higher  $R_f$  the metallic phase disappears. The content of metallic Bi into oxyfluoride matrix can be tuned by  $R_f$ , but also by the target applied power or by varying only one reactive gas flow rate. By increasing the film thickness, the composition stays stable but the phase crystallization is enhanced. Hence, we succeed to form in one-step Bi/BiO<sub>0.5</sub>F<sub>2</sub> heterojunctions, where the metal presence improves the light absorption, the photogenerated carrier separation, and thus the photocatalytic efficiency for MO degradation in water. For all these conditions, the film obtained with  $R_f = 0.3$  and  $t_d = 20$  min seems to correspond to an optimal composition. Indeed, 90 % of MO was degraded after 2 hours of irradiation in the presence of this film, which is stable after 3 photocatalytic cycles ( $\approx 9$  hours). This heterojunction is also efficient to photoreduce CO<sub>2</sub> with a photoproduction rate of 25  $\mu\text{mol/h/g}$  and a selectivity for CO at 70%.

## Keywords

Bismuth oxyfluoride thin films, plasmonic Bi<sup>0</sup>/BiO<sub>0.5</sub>F<sub>2</sub> heterojunction structure, reactive magnetron sputtering, methyl orange photodegradation, CO<sub>2</sub> photoconversion.

## 1. Introduction

Heterogeneous photocatalysis has been considered as a hot research topic to solve environmental problems and energy losses since the first report by Fujishima and Honda [1]. Photocatalysis uses the UV or visible light irradiation for environmental remediation (pollutant degradation) and clean energy production (hydrogen production and carbon dioxide (CO<sub>2</sub>) reduction) [2]. Among the different classes of materials, titanium dioxide (TiO<sub>2</sub>) [3-7], zinc oxide (ZnO) [8-10], graphite-like carbon nitride (g-C<sub>3</sub>N<sub>4</sub>) [11-13], and bismuth-based materials [2,14-17] have been widely employed in a variety of environmental and energy photocatalytic reactions. Bismuth oxyhalides, BiOX (X: Cl, Br, I), have lately emerged as a new family of promising photocatalysts. Indeed, BiOX exhibits a unique layered structure characterized by fluorite-like [Bi<sub>2</sub>O<sub>2</sub>]<sup>2+</sup> slabs interleaved by double slabs of halogenide anions. The internal electric fields (IEF) between [Bi<sub>2</sub>O<sub>2</sub>] slabs and the anionic halogen layers induce the efficient separation of the photoexcited charge carriers and reveal the potential photocatalytic performance of BiOX [17,18]. Unlike the other bismuth oxyhalides, bismuth oxyfluoride (BiOF) material exhibits a direct band gap of 4.2 eV in the UV light range. Thus, for a long time, fluorinated bismuth derivative compounds were not considered as interesting materials for photocatalytic applications due to their high band gap, which explains why only a few studies have been done compared to the other bismuth-based halide compounds [19,20]. Recently, bismuth oxyfluoride materials have attracted significant attention since fluorine has distinctive chemistry properties from chlorine, bromine, and iodine. Due to its high electronegativity, fluorine can trap electrons firmly leading to an uneven electron distribution

and enhancing the photocatalytic efficiency [21]. Yet, the photocatalytic activity of BiOF could be further improved by different approaches. For instance, the construction of heterojunction structures such as Ag<sub>2</sub>O/BiOF [22], BiOBr/BiOF [23] and BiOCl/BiOF [19] strengthens the visible light response, promotes the separation of the photogenerated charge carriers, and thus enhances the photocatalytic activity. Moreover, Bi<sub>x</sub>O<sub>y</sub>F<sub>z</sub> compounds with different atomic ratios have been reported as efficient photocatalysts. The different O/F ratios in BiO<sub>0.51</sub>F<sub>1.98</sub> (O/F = 0.25), BiO<sub>0.9</sub>F<sub>2.35</sub> (O/F = 0.38), and BiO<sub>0.67</sub>F<sub>1.66</sub> (O/F = 0.4) could be responsible for the variation in the intensities of the internal electric fields. As the O/F ratio decreases, the amount of oxygen defects decreases, and the photocatalytic activity of Bi<sub>x</sub>O<sub>y</sub>F<sub>z</sub> increases. Therefore, Bi<sub>x</sub>O<sub>y</sub>F<sub>z</sub> materials with different O/F molar ratios exhibit better photocatalytic activity than the stoichiometric BiOF [24,25]. In this work, we investigate the deposition of oxyfluoride thin films by reactive magnetron sputtering of a pure Bismuth target in Ar/O<sub>2</sub>/CF<sub>4</sub> atmosphere and teste them for gas CO<sub>2</sub> photoconversion and for pollutant photodegradation in water. For the latter application, thin films are more favorable for their reusability and recovery without the need for filtration or any other sophisticated separation technique [26]. Moreover, to our knowledge, the synthesis of bismuth oxyfluoride films by sputtering has not been reported in the literature so far. Thus, the originality of this work arises from the deposition of novel photocatalytic bismuth oxyfluoride thin films by this technique.

## 2. Materials and methods

### 2.1. Thin films deposition

Bismuth oxyfluoride films were grown by reactive sputtering of a Bismuth target (99.99% purity and a size of 76 x 3 mm) in Ar/O<sub>2</sub>/CF<sub>4</sub> atmosphere onto different substrates including

silicon, quartz, and vitreous carbon. Initially, the substrates were ultrasonically cleaned in water, ethanol, and acetone for 30 min each and then dried using compressed air. Subsequently, they were placed in the vacuum chamber on a substrate holder that was rotated at five rotations per minute (rpm) without heating nor biasing. The substrate was positioned above the target with a separation distance of 13.5 cm. The system was kept under vacuum, reaching a base pressure of about  $10^{-6}$  mbar. Before any sputtering experiment, the target was sputter-cleaned in argon plasma. A first set of films was deposited at room temperature with a fixed deposition time of 3 min, a radiofrequency (13.56 MHz) power of 50 W, a working pressure of  $2.2 \times 10^{-2}$  mbar. The total flow rate ( $\Phi_{\text{Ar}} + \Phi_{\text{O}_2} + \Phi_{\text{CF}_4}$ ), where  $\Phi_{\text{Ar}}$ ,  $\Phi_{\text{O}_2}$  and  $\Phi_{\text{CF}_4}$  are flow rate for Ar, O<sub>2</sub> and CF<sub>4</sub> respectively, is kept constant at 30 standard cubic centimeters per minute (sccm); while the reactive gas ratio ( $R_f = \Phi_{\text{O}_2}/(\Phi_{\text{O}_2} + \Phi_{\text{CF}_4})$ ) is varied from 0 to 0.6. A second set of films were obtained varying the rf power (50-100 W), the O<sub>2</sub> and CF<sub>4</sub> flow rates, and the deposition time (3-30 min).

## **2.2. Thin films characterization**

The elemental analysis of the films deposited on vitreous carbon substrate was investigated by Rutherford Backscattering Spectrometry (RBS) at CEMHTI-CNRS (Orléans, France), using 2 MeV alpha particles. The experimental spectra were simulated with SIMNRA program to determine the concentrations of Bi, O, F, and C elements.

However, the quantification of carbon in the films that may come from the dissociation of CF<sub>4</sub> was not so accurate. Therefore, the carbon content in the films was estimated by X-ray photoelectron spectroscopy (XPS). XPS uses the Omicron brand EA 125 model with a DAR 400 X source. It utilizes the MgK <sub>$\alpha$</sub>  anode ( $E = 1253.6$  eV) and a hemispheric analyzer working at constant energy of 20 eV for the acquisition of high-resolution spectra. A high-resolution

measurement was made for Bi4f, O1s, F1s, and C1s peaks. After the acquisition, the exploitation of the experimental data was carried out by the XPSPEAK41 software. First, a Shirley baseline was used to subtract the background level on the spectra. The experimental spectra were then calibrated in energy by setting the adventitious C 1s (C-C) at 285.12 eV in agreement with reference [27].

The crystal structure of the films deposited on Si (100) was investigated by X-ray diffraction, PANalytical XPert'PRO diffractometer model ( $\text{CuK}\alpha_1$  1.5406 Å,  $\text{CuK}\alpha_2$  1.5444 Å°, 40 kV, 30 mA, and an angle step of 0.0167°).

The Raman spectroscopy measurements were done at room temperature using a Jobin-Yvon T64000 spectrometer on thin films deposited on vitreous carbon. A laser emits light at 514.5 nm with a minimum power of 50 mW, such that the power reaching the sample is ~ 200 µW, which doesn't result in local annealing. Data acquisition was made with Labspec software.

The apparatus used for Fourier Transform Infra-Red spectroscopy (FTIR) analysis is the Nicolet 5700 Fourier spectrometer in the frequency range 4000-400  $\text{cm}^{-1}$  with a scan number of 80 and a resolution of 4  $\text{cm}^{-1}$ . Data acquisition was made with omnic software such that a measurement of the double-side polished intrinsic Si (100) substrate alone was necessary to subtract its contribution. The measured intensities were then normalized by the thickness of the films to eliminate the influence of the material's quantity.

In order to get a local characterization of the films, high resolution transmission electron microscopy (HR-TEM) was carried out using a S/TEM Themis Z Thermo Fisher Scientific, 300kV. HR imaging was performed to observe the nanoscale nature of the crystallized particles and phase identification was conducted using selected area electron diffraction on chosen crystallized particles. Comparison with the expected diffraction planes confirmed the nature of bismuth oxy-fluoride. The observation of metallic bismuth was not possible due to the sublimation of the metal under the electron beam.

### 2.3. Thin films optical properties

The thickness and the optical indexes of the films were investigated by spectroscopic ellipsometry thanks to an ex-situ Jobin-Yvon Uvisel ellipsometer that utilizes a 125 W Xenon arc lamp, an IHR 320 monochromator, UV-Vis and infra-red photomultipliers allowing measurement in the range of 0.59 to 4.96 eV. Information was deduced from the simulation of the measured ellipsometric angles ( $\Psi$  and  $\Delta$ ) using the DeltaPsi2 software.

The transmittance (T) of the films deposited on a transparent quartz substrate was measured by a UV-Visible spectrophotometer UV-2600 Shimadzu model over a range of wavelengths between 200 and 800 nm using the UVProbe software. The absorption coefficient ( $\alpha$ ) was calculated from the transmittance by means of Lambert-Beer's law and from film thickness deduced from ellipsometry. The UV-visible spectrum was then used to determine the band gap ( $E_g$ ) of semiconductors through Tauc plot, which relates the band gap and the absorption coefficient as shown in Equation 1,

$$(\alpha h\nu)^{1/n} = B(h\nu - E_g) \quad (1)$$

n is an index that characterizes the optical absorption process, it equals to 1/2 or 2 for direct or indirect allowed transitions, respectively;  $h\nu$  is the photon energy (eV), and B is a proportionality constant known as the band tailing parameter ( $B = 1$ ).

### 2.4. Thin films' photocatalytic properties

First, the photocatalytic activity of bismuth oxyfluoride films was investigated by measuring the evolution of the absorbance spectrum of an aqueous solution of  $5.2 \times 10^{-5}$  mol L<sup>-1</sup> of methyl orange dye (MO) as a function of the irradiation time. The deposited film was placed

vertically at the bottom of the cell containing 3 mL of MO solution and stirred under darkness for 60 minutes to establish equilibrium between the dye and the photocatalyst. Then, the cell containing the film was placed at a distance of about 20 cm from a 1000 W Xenon (Xe) lamp that emits light from 200 to 900 nm. Continuous stirring was maintained to have homogeneity between the dye and the catalyst. The UV-Vis measurements were carried out every 20 min up to 120 min and then every 60 min up to 240 min. The pseudo-first-order reaction rate of the samples (k) was obtained using the Langmuir–Hinshelwood model by plotting  $\ln(A_o/A)$  as a function of the irradiation time. Hence, the slope of such plot corresponds to k according to Equation 2.

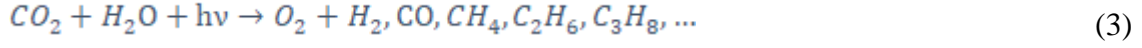
$$\ln\left(\frac{A_o}{A}\right) = kt \quad (2)$$

The values of k were then normalized by the surface area of films to eliminate the geometrical surface's effect between samples that could slightly differ from size.

Secondly, the ability of bismuth oxyfluoride material in reducing CO<sub>2</sub> was explored at IFPEN (Solaize, France). The photoconversion experiments were carried out continuously in a stainless-steel fixed bed reactor gas flow passing through the sample, operating at atmospheric pressure and controlled temperature of 30 °C. The CO<sub>2</sub>/H<sub>2</sub>O molar ratio (obtained by CO<sub>2</sub> bubbling in a thermalized water tank) was fixed at 24, and the CO<sub>2</sub> gas flow rate was set at 0.3 cubic centimeters per minute (cc.min<sup>-1</sup>). A Xe lamp Max303 Asahi provided the UV-Visible irradiation from 280 to 620 nm. The irradiance was controlled with a radiometer equipped with CCD captor (Delta Ohm) and adjusted to 80 W.m<sup>-2</sup> for 315-400 nm wavelength range. Moreover, the reactor has an optical quartz window through which the light flux reached the material. The catalyst was supported on a filter inside the Teflon ring, where the film was crushed to obtain powder where the gas could go through. Reagents and products were then



analyzed on-line by a gas chromatograph TCD sensor microchromatograph Lan3000 (SRA Instruments,  $\mu$ GC-TCD). Gas-phase analyses were performed every 10 minutes during 20 hours. According to Equation 3, the simplified unbalanced reaction with all the reactants and products in the gas phase, a couple of products could be obtained.



Then, to evaluate the photocatalytic performance of the materials for CO<sub>2</sub> reduction, the calculated parameters must consider all the products. Two parameters are then defined: the average electron consumption rate Equation (4) and the average selectivity (Equation (5)), calculated after 20 hours of Time On Stream (T.O.S.).

$$\bar{r}_m^{\bar{e}} = \frac{1}{T.O.S.} \int_0^{T.O.S.} \sum_i \frac{n_i^{\bar{e}}[i](t) \cdot Q_{tot}}{V_{m,m}} \cdot 60 \, dt \quad (4)$$

$$\bar{S}_i^{\bar{e}} = \frac{1}{T.O.S.} \int_0^{T.O.S.} \frac{n_i^{\bar{e}}[i](t)}{\sum_j n_j^{\bar{e}}[j](t)} \, dt \quad (5)$$

Where,  $n_{i,j}^{\bar{e}}$  is the stoichiometric coefficient of the electrons consumed by the product i (for example, 2  $\bar{e}$  are needed to form H<sub>2</sub> or CO, whereas CH<sub>4</sub> needs 8  $\bar{e}$ ),  $\left[ \begin{matrix} i \\ j \end{matrix} \right] (t)$  is the concentration of product i (or j) over time (in ppmVol), Q<sub>tot</sub> is CO<sub>2</sub> and H<sub>2</sub>O input flow rates (3.09 x 10<sup>-4</sup> L.min<sup>-1</sup>), and V<sub>m</sub> is the molar volume of a gas at 25°C (24.5 L.mol<sup>-1</sup>). Average electron consumptions are given with a standard deviation of approximately  $\pm 10\%$ .

### 3. Results and discussion

#### 3.1. Influence of the reactive gas ratio (R<sub>f</sub>)

In order to investigate the synthesis of bismuth oxyfluoride thin films by reactive sputtering, the reactive gas ratio, R<sub>f</sub>, corresponding to the O<sub>2</sub> flow rate to the total reactive gas (O<sub>2</sub> + CF<sub>4</sub>) flow rate ratio is varied from 0 to 0.6. Other process parameters are kept constant: 29 sccm for the argon flow rate, 1 sccm for the total reactive gas flow rate, a rf power of 50W on the pure Bi target and a deposition time of 3 min. Figure 1a shows the XRD patterns of the films

deposited depending on  $R_f$  to identify the synthesized phases. The Figure 1b presents a zoom on the main peak of the films (around  $26-27^\circ$ ) compared to the patterns of numerous bismuth compounds: Bi,  $\text{Bi}_2\text{O}_3$ , BiOF,  $\text{BiO}_{0.5}\text{F}_2$ ,  $\text{Bi}_7\text{O}_5\text{F}_{11}$ ,  $\text{BiF}_3$ . Results reveal that the films deposited at  $0 \leq R_f \leq 0.5$  consist of two phases:  $\text{BiO}_{0.5}\text{F}_2$  and metallic bismuth. Indeed, the peaks appearing at  $2\theta = 26.4^\circ$ ,  $30.4^\circ$ ,  $43.6^\circ$ , and  $51.8^\circ$  correspond to the (111), (200), (220), and (311) planes of  $\text{BiO}_{0.5}\text{F}_2$  [28]; while the peak at  $27.2^\circ$  is attributed to the (012) plane of Bi [29]. The presence of metallic Bi indicates that the amount of the injected reactive gases ( $\text{O}_2$  and  $\text{CF}_4$ ) is not high enough to react with all the sputtered bismuth atoms, leaving some metallic parts in the oxyfluoride matrix. We may notice that  $\text{BiO}_{0.5}\text{F}_2$  is not the most common oxyfluoride phase. Figure 2a presents the intensity of the main peaks for  $\text{BiO}_{0.5}\text{F}_2$  and Bi phases, normalized by film thickness, as a function of  $R_f$ . We observe a global decrease of these phases in the films until  $R_f = 0.6$ , where they are no more observed. For  $R_f = 0.6$ , the peak appearing at  $2\theta = 26.2^\circ$  on Figure 1 is attributed to the (111) plane of  $\text{BiF}_3$  phase. Of course, depositing a pure fluoride thin film is difficult to explain with an  $\text{O}_2$ -containing gas mixture; that is why we assume the presence of an amorphous oxide compound in this film, not detectable by XRD. With this gas mixture, metallic Bi is no more present indicating that all the Bi atoms sputtered from the target are oxidized or fluorinated by the reactive gases. In parallel to this new  $\text{BiF}_3$  phase, Figure 2b shows a drop in the thickness, deduced from ellipsometry, from 80-90 nm for  $R_f \leq 0.5$  to around 40 nm for  $R_f = 0.6$ , suggesting a shift of the process from a metallic to a compound sputtering mode.

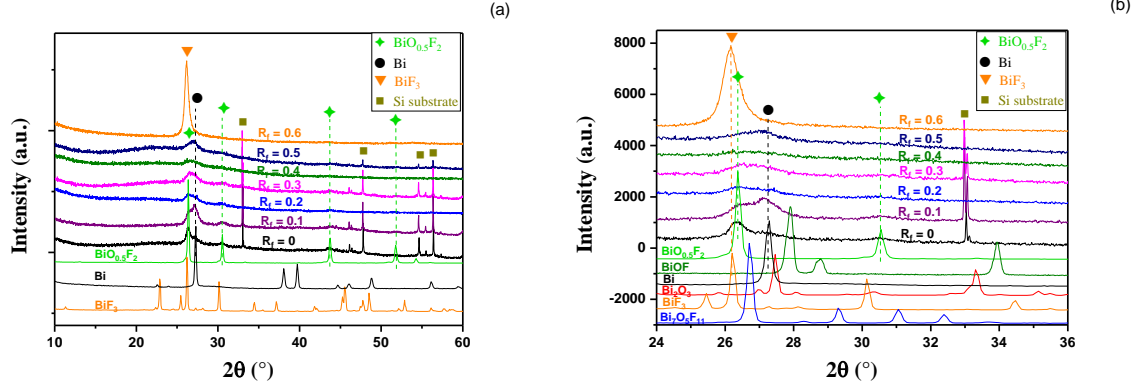


Figure 1: XRD patterns of bismuth oxyfluoride films deposited with  $R_f = 0-0.6$ .

Figure 2b shows the composition of the films deduced from RBS analysis. For all films, the percentage of bismuth is approximately constant ( $\sim 30\%$ ); whereas F content slightly decreases and O content slightly increases with  $R_f$ . The relatively high content of oxygen, while XRD shown the presence of oxygen-poor phases ( $\text{BiO}_{0.5}\text{F}_2$ , Bi and  $\text{BiF}_3$ ), confirms that amorphous bismuth oxide phases should be present into the samples. We may also remark the very low percentage of carbon in the films; whereas carbon atoms are provided from injected  $\text{CF}_4$  molecules. This can be explained by the etching of carbon in the growing films by oxygen radicals from plasma, already observed in literature [30]. However, it is difficult to quantify precisely by RBS the proportion of carbon in the films, since they are deposited on a vitreous carbon substrate. Accordingly, this aspect should be confirmed latter by XPS.

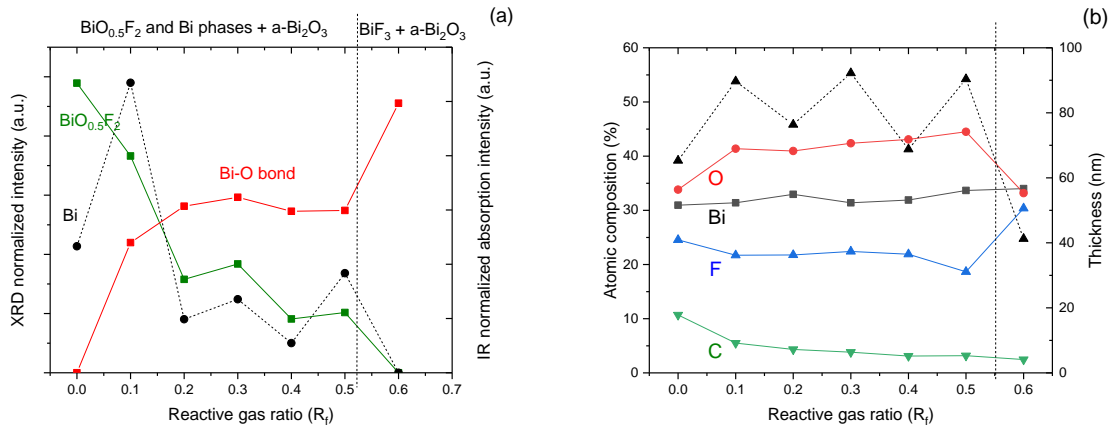


Figure 2: (a) Normalized intensities of (111)  $\text{BiO}_{0.5}\text{F}_2$  and (012) Bi XRD peaks and of Bi-O bonds IR absorption at  $612\text{ cm}^{-1}$ , and (b) elemental composition of bismuth oxyfluoride films and their thickness for a 3 min deposition time, as a function of the reactive gas ratio,  $R_f$ .

To better quantitatively evaluate the presence of amorphous compounds, especially bismuth oxide, we investigate the deposited films by Raman and IR spectroscopies. The FTIR and Raman spectra are shown in Figure S1 in supplementary information. For both techniques, the measured spectra are as expected. The IR bands detected in the 700 - 400  $\text{cm}^{-1}$  range, especially the main one at 612  $\text{cm}^{-1}$ , correspond to the Bi-O stretching vibrations in bismuth oxide and/or oxyfluoride films [31]. For  $R_f = 0$  ( $\Phi_{\text{CF}_4} = 1$  sccm), the intensity of these peaks is very low and a peak at 453  $\text{cm}^{-1}$  emerges. The latter could be attributed to the stretching vibrations of Bi-F bonds [28]. The peak at 840  $\text{cm}^{-1}$  refers to Bi-O-Bi symmetric stretching vibrations in  $\text{Bi}_2\text{O}_3$  but also in  $\text{BiO}_{0.5}\text{F}_2$  [32]. The presence of fluorine is also confirmed by the small C-F vibration band observed at 1122  $\text{cm}^{-1}$  [33]. For Raman spectra, the bands observed at 126  $\text{cm}^{-1}$  could be assigned to Bi-O and Bi-F stretching vibrations, while the stretching and bending vibrations of Bi-O-Bi and Bi-F-Bi appear at around 314  $\text{cm}^{-1}$ , but they are not easily distinguished [34]. The band at 624  $\text{cm}^{-1}$  could be attributed to  $\text{Bi-O}^-$  [35]. Moreover, the presence of metallic bismuth is observed by the Bi-Bi vibration band at 95  $\text{cm}^{-1}$  but its intensity could not be precisely determined due to some apparatus limitation in this region [36]. Finally, the normalized contributions of Bi-O bonds at 612  $\text{cm}^{-1}$  from IR were added to Figure 2a. This band can be attributed to both  $\text{BiO}_{0.5}\text{F}_2$  and  $\text{Bi}_2\text{O}_3$  compounds. However, its intensity is very low for  $R_f = 0$  while diffraction peaks indicate the presence of  $\text{BiO}_{0.5}\text{F}_2$  phase in this film. Hence, the main contribution to this Bi-O band seems to be the  $\text{Bi}_2\text{O}_3$  compound. When  $R_f$  increases, we observe a progressive increase of Bi-O bonds content, which is linked to the increasing part of amorphous  $\text{Bi}_2\text{O}_3$ . Hence, for  $R_f$  values between 0 to 0.5, the deposited films are composed of a decreasing part of crystallized  $\text{BiO}_{0.5}\text{F}_2$  and Bi phases in mixture with slightly increasing part of amorphous  $\text{Bi}_2\text{O}_3$ . For  $R_f = 0.6$ , the previous  $\text{BiO}_{0.5}\text{F}_2$  and Bi phases disappear, the Bi-O band intensity drastically increases, indicating higher part of amorphous  $\text{Bi}_2\text{O}_3$  in parallel to a  $\text{BiF}_3$  phase emergence. For this  $R_f$ , a phase segregation of

the oxyfluoride compound is then observed in a mixture of crystallized  $\text{BiF}_3$  phase and amorphous  $\text{Bi}_2\text{O}_3$ .

We then explored the optical properties of the films thanks to UV-visible spectroscopy and ellipsometry. The variation of the films transmittance measured by UV-visible spectroscopy is displayed in Figure 3a. Films deposited at  $R_f \leq 0.5$  exhibit low transmittance in the UV-visible range due to their metallic bismuth content, whereas the film deposited at  $R_f = 0.6$  is more transparent in visible range. These results are confirmed by the simulation of the extinction coefficient,  $k$ , from ellipsometric measurements, plotted in Figure 3b. For  $R_f = 0.6$ , a simple Tauc-Lorentz model is used to fit the measurements. Hence, the extinction coefficient is null for photon energy lower than the band gap and drastically increases at higher energies. This is in agreement with the insulator behavior of  $\text{BiF}_3$  or  $\text{Bi}_2\text{O}_3$  compounds. For lower  $R_f$ , a Lorentz oscillator should be added to the previous model, considering light absorption at low photon energy due to the presence of metallic Bi. The obtained  $k$  is now composed of two parts: an absorption at energy higher than 3.5 eV, due to band gap of  $\text{BiO}_{0.5}\text{F}_2$  or  $\text{Bi}_2\text{O}_3$  compounds, and a new and large absorption around 1 eV, due to the presence of metallic Bi. From both techniques, UV-visible spectroscopy and ellipsometry, the band gap values were resolved and plotted in Figure 3c. The films exhibit a direct band gap [24,37], with values ranging from 3.89 to 4.33 eV from ellipsometry results. Values obtained from UV-visible are close even if they are less precise because of the high contribution of Bi to the absorbance. These values are lower than the one reported for  $\text{BiO}_{0.5}\text{F}_2$ , which can be explained by the presence of metallic Bi. Indeed, a slight band gap decrease was already reported due to metallic bismuth addition in the  $\text{Bi}_2\text{WO}_6/\text{Bi}$  system [38]. We might also remark, that the band gap is minimum for  $R_f = 0.3$ , which could be favorable for photocatalysis.

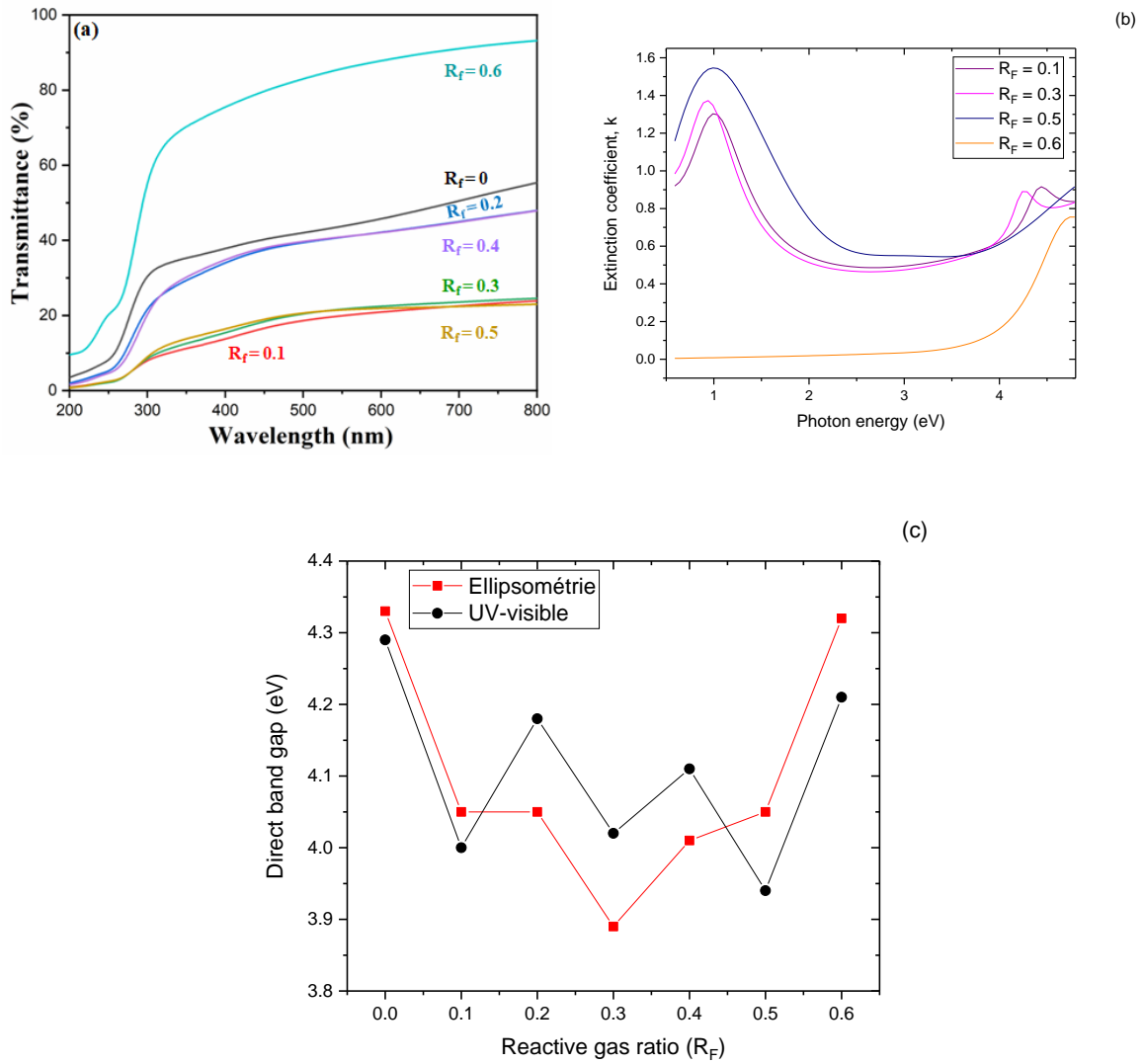


Figure 3: (a) Films transmittance from UV-visible absorption spectroscopy, (b) extinction coefficient from ellipsometry and (c) band gaps determination from both techniques.

Figure 4a presents the degradation of MO in water without any photocatalysts and in the presence of the films deposited at  $R_f = 0.2, 0.3$ , and  $0.6$ . First of all, interestingly, we observed that all the deposited films present a photocatalytic activity. We also compare film performance to pure oxyfluoride phase, by studying the degradation of MO with 1.28 mg of  $\text{BiO}_{0.5}\text{F}_2$  powder. This mass was chosen to be twice the estimated mass of our films ( $\sim 0.7$  mg). Results show that even if the powder amount is twice higher, our films composed of a  $\text{BiO}_{0.5}\text{F}_2/\text{Bi}$  mixture, for  $0 \leq R_f \leq 0.5$ , exhibits better photocatalytic performance. In Figure 4b,

we plotted the reaction rate,  $k$ , divided by the geometrical surface area of the film, S.A., in order to eliminate the effect of sample size variation. For  $0 \leq R_f \leq 0.5$ , the film deposited at  $R_f = 0.3$  seems to exhibit the highest performance, in agreement with its lower band gap. We also observed a good reaction rate,  $k/SA$ , for the film at  $R_f = 0.6$ . However, it is difficult to compare this latter result to the other one since the present phases are different. Interestingly, the best film ( $R_f = 0.3$ ) is not the one with the highest  $\text{BiO}_{0.5}\text{F}_2$  crystallinity ( $R_f = 0.0$ ). Similar results were observed with the  $\text{Bi}_2\text{O}_3/\text{Bi}$  system, for which an enhanced photocatalytic activity for MO photodegradation was demonstrated by the addition of a controlled Bi content [29]. This has been interpreted as a heterojunction effect to increase the separation of the photogenerated carrier and / or an improved light absorption due to plasmonic effect of metallic nanodomains. Of course, a too high amount of metallic Bi will also lead to a decrease of light absorbed by the photocatalyst, which will reduce its activity. Hence, a compromise between both phases needs to be found. Here, the optimum ratio seems to occur at  $R_f = 0.3$ . However, photocatalytic performance may be increased by enlarging the investigated process parameters around this promising condition.

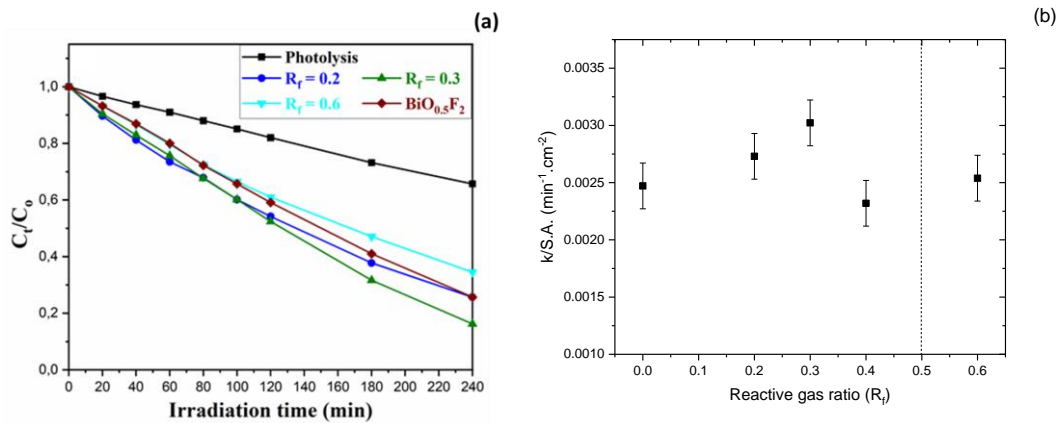


Figure 4: (a) Degradation of MO ( $C_t/C_0$ ) as a function of the irradiation time in the presence of films ( $R_f = 0.2$ , 0.3, and 0.6) and  $\text{BiO}_{0.5}\text{F}_2$  powder, and (b) the reaction rate to surface area,  $k/SA$ , as a function of  $R_f$ .

### 3.2. Influence of discharge power and flow rates parameters

In a second set of measurements, the previous condition at  $R_f = 0.3$  is taken as a reference and some process parameters are modified. First, in order to explore the effect of a higher content of metallic Bi, we increase the rf power applied to the target from 50W (reference sample) to 75 and 100W. The XRD patterns obtained for these films are plotted on Figure 5a and shows an increase of metallic Bi peak intensity detrimentally to the  $\text{BiO}_{0.5}\text{F}_2$  ones. In these conditions, when the rf power is increased, the flux of Bi atoms reaching the substrate is increased; while the constant amount of reactive gases is not high enough to react with all the sputtered atoms, leading to incorporate more metallic Bi. However, this higher Bi content is accompanied by a decrease of the photocatalytic response:  $k/\text{SA}$  drops to values lower than  $2.10^{-3} \text{ min}^{-1}.\text{cm}^{-2}$ .

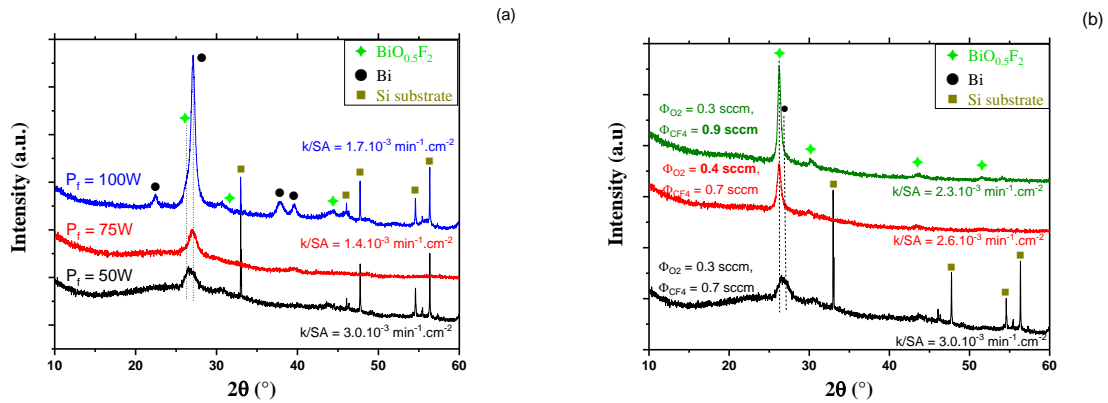


Figure 5: XRD patterns for thin films deposited (a) at fixed gas mixture of 0.3 sccm of  $\text{O}_2$  and 0.7 sccm of  $\text{CF}_4$  (also called  $R_f = 0.3$ ) and various rf power and (b) at fixed rf power of 50W and various gas mixture.

At the opposite, at a fixed 50 W power, increasing the flow rate of  $\text{O}_2$  (to 0.4 sccm) or  $\text{CF}_4$  (to 0.4 sccm) flow rates allows us to decrease the metallic content and drastically increase the crystallization of oxyfluoride phase in the films, as shown in Figure 5b. However, whatever the improvement of  $\text{BiO}_{0.5}\text{F}_2$  crystallinity, the reduction of Bi content seems to limit the film photocatalytic performance ( $k/\text{S.A.} < 3.10^{-3} \text{ min}^{-1}.\text{cm}^{-2}$ ). Finally, even if these various process



parameters allow one to finely controlled the content of both phases, the film previously obtained at  $R_f = 0.3$  seems to be the best compromise for optimal photocatalytic properties.

### 3.3. Influence of the deposition time

Since the ratio between both phases seems to be the best for  $R_f = 0.3$ , we might try to increase the crystallinity part without varying their ratio. Previous thin films present a limited crystallization that could be due to their limited thickness ( $< 100$  nm). We then tried to favor phases crystallization by increasing the deposition time. Figure 6a presents the thickness variation as a function of the deposition time. The first exciting remark is that the variation is not linear. Initially, the deposition rate is around 30 nm/min for deposition time of 3 min. It then decreases to 22-25 nm/min for longer time. This could be a sign of film densification due to its crystallization.

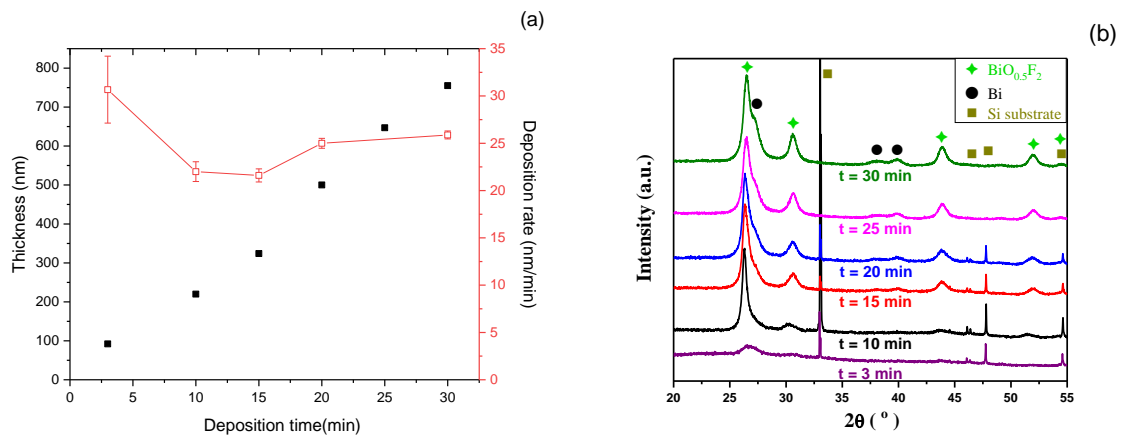


Figure 6: (a) The thickness and deposition rate of bismuth oxyfluoride films ( $R_f = 0.3$ ) as a function of the deposition time, and (b) the XRD patterns of these films.

The XRD patterns of bismuth oxyfluoride films deposited at different deposition time are shown in Figure 6b. These results confirm that by increasing the deposition, from 3 to 10 min, the global intensities of the diffraction peaks are enhanced. The XRD patterns also confirm that at  $R_f = 0.3$ , films are all composed of a mixture of  $\text{BiO}_{0.5}\text{F}_2$  and Bi. No other crystallized phase is observed, even if we cannot exclude the presence of amorphous compound. The film

surface roughness was also evaluated. As expected, the thickness and crystallization enhancement with deposition time leads to higher roughness. However, this increase stays moderate: from  $R_q = 2$  nm for 3 min deposition to 10 nm for 30 min.

To investigate the film microstructure more in detail, we performed some SEM and HR-TEM analysis. Images for the film deposited at  $R_f = 0.3$  and  $t_d = 20$  min are shown in Figure 7. First, SEM images from top and trench on Figure 7a show a porous structure with a rough surface, in agreement with the AFM measurements. When this film is scratched on TEM grid, we remark that it is composed of small grains, where their size is found to be  $\sim 10$  nm, and that oxyfluoride phase is the  $\text{BiO}_{0.5}\text{F}_2$  one. Unfortunately, Bi grains cannot be studied by TEM because of their low melting point. Indeed, this lead to the grain melting under the electron beam, which modifies their shape and size before observation.

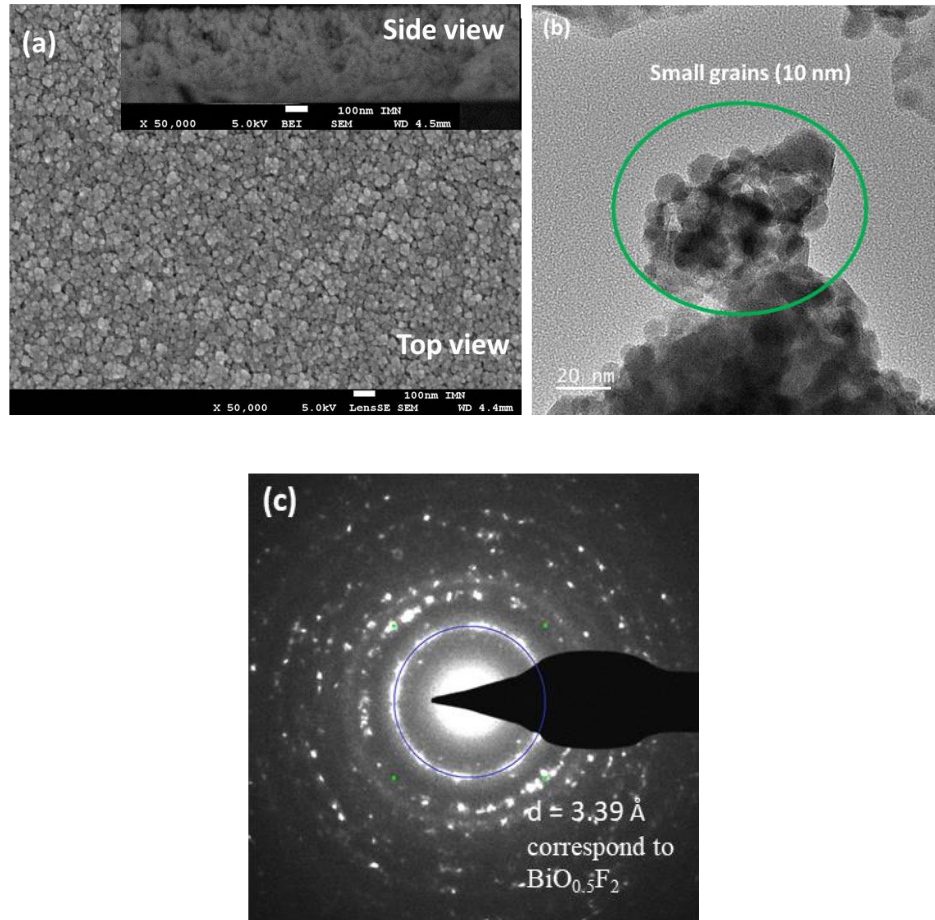


Figure 7: Microscopy images of the film deposited at  $R_f = 0.3$  and  $t_d = 20$  min. (a) SEM pictures of top and side view, (b) TEM images. Small grains of  $\sim 10$  nm size are observed. (c) SAED pattern of nanoscale particles located in the circle. The distance of  $3.39 \text{ \AA}$  corresponds to the (111) plane of  $\text{BiO}_{0.5}\text{F}_2$ .

To quantify the potential presence of amorphous bismuth oxide and to check the low content of carbon into our films, XPS analysis was carried out on the same film. Figure 8 presents the XPS high resolution spectra for C 1s, Bi 4f, O 1s and F 1s binding energies. Since the binding energies for various oxyfluoride are relatively close, XPS spectra measured with pure  $\text{BiO}_{0.5}\text{F}_2$  powder were added to Figure 8. The binding energies of 159.7 and 165.0 eV correspond to Bi 4f<sub>7/2</sub> and Bi 4f<sub>5/2</sub>, respectively, consistent with the Bi<sup>3+</sup> oxidation state in  $\text{BiO}_{0.5}\text{F}_2$  [39]. The small second doublet appearing at lower binding energies in thin film is assigned to the metallic Bi<sup>0</sup> chemical state, in agreement with the XRD results. The high-resolution XPS spectrum of O1s is decomposed into three peaks, where the peaks at 530.32, 531.73, and 532.77 eV correspond to Bi-O, C=O, and C-O bonds, respectively [31]. The peak at 684.03 can be attributed to the F species in  $\text{BiO}_{0.5}\text{F}_2$  [40]. Hence, the XPS peaks detected at 159.7, 530.32, and 684.03, corresponding to Bi 4f<sub>7/2</sub>, O 1s, and F 1s, respectively, could be referred to  $\text{BiO}_{0.5}\text{F}_2$  material as reported in literature [41]. We remark, that these peaks are also in agreement with those measured on  $\text{BiO}_{0.5}\text{F}_2$  powder.

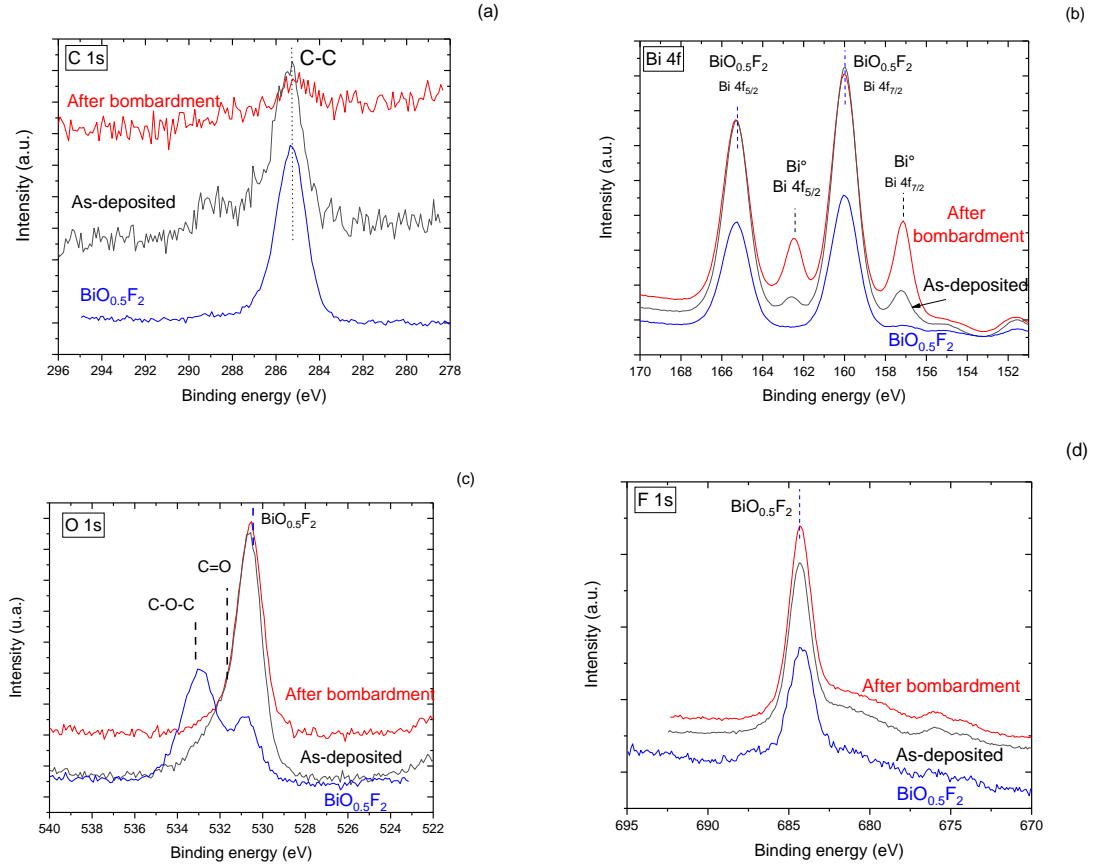


Figure 8: XPS spectra obtained for (a) C 1s, (b) Bi 4f, (c) O 1s and (d) F 1s for film deposited at  $R_f = 0.3$  for 20 min, before and after  $\text{Ar}^+$  bombardment and for  $\text{BiO}_{0.5}\text{F}_2$  powder.

In Figure 8a, a weak C 1s peak is observed for the film. The three peaks emerging at 285.12, 286.62, and 288.62 eV are ascribed to C-C, C-O, and O-C=O bonds, respectively [27]. No peak at energy higher than 289.5 eV, corresponding to  $\text{C-F}_x$  environments, is seen. A first elemental quantification, reported on Table 1, estimates the carbon content to around 11%. However, in our case, it is difficult to specify if this carbon originates from dusts on the surface or from carbon from  $\text{CF}_4$  reactive gas incorporated into the film during its growth. To answer this question, we clean the film surface thanks to low energy  $\text{Ar}^+$  ion bombardment ( $E = 1 \text{ keV}$ ,  $I = 10 \mu\text{A}$ , for 2 min). The analysis made after this bombardment is also presented in Figure 8. After bombardment, compared to the original film, the same peaks are observed; but the carbon peak is drastically reduced from 11 to 2% of elemental composition (see Table 1); whereas other peaks are rather unchanged. Indeed, most of the initially detected carbon

originates from adventitious carbon, as classically observed on sample surface analyzed by XPS, and only few percent are from carbon incorporated into the thin film. This low carbon content, in agreement with RBS results (%C = 4 at.% for  $R_F = 0.3$ ), might be explained by an etching effect by O radicals from the plasma in Ar/O<sub>2</sub>/CF<sub>4</sub> mixture.

**Table 1: The elemental composition, formula and phases content calculation for the bismuth oxyfluoride film deposited at  $R_F = 0.3$  for 20 min, before and after bombardment with Ar<sup>+</sup> ions.**

|               | Elemental composition         |      |      |      |                                       | Phases for Bi environment         |      |                                |
|---------------|-------------------------------|------|------|------|---------------------------------------|-----------------------------------|------|--------------------------------|
|               | Bi                            | O    | F    | C    | Formula                               | BiO <sub>0.5</sub> F <sub>2</sub> | Bi   | Bi <sub>2</sub> O <sub>3</sub> |
| Pristine      | 31.7                          | 19.0 | 38.6 | 10.6 | BiO <sub>0.59</sub> F <sub>1.20</sub> | 60.2                              | 35.4 | 4.4                            |
| After etching | 38.3                          | 14.7 | 44.6 | 2.4  | BiO <sub>0.38</sub> F <sub>1.16</sub> | 58.4                              | 38.3 | 3.2                            |
|               | From Bi 4f peak decomposition |      |      |      |                                       | 67.6                              | 27.8 | 4.6                            |

On the Bi 4f spectrum, the Bi<sub>2</sub>O<sub>3</sub> phase, whose peak Bi 4f<sub>7/2</sub> is reported at 158.7 eV, cannot be clearly seen, indicating its amount should be low. However, we may take into account the presence of this phase into Bi 4f peak decomposition, shown in Figure 9. From peak areas, Bi environment is evaluated to be at 28 % of Bi, 68 % of BiO<sub>0.5</sub>F<sub>2</sub> and 4-5 % of Bi<sub>2</sub>O<sub>3</sub> (reported in Table 1). Details of peak position, width and area can be found in supplementary information. However, since the Bi<sub>2</sub>O<sub>3</sub> peak is very close to the BiO<sub>0.5</sub>F<sub>2</sub> one, its contribution part, obtained from data fitting, can be imprecise. To confirm the latter results, we calculate the contributions of the three phases from the global elemental composition, which is not influenced by peak fitting. We considered that all F atoms are from BiO<sub>0.5</sub>F<sub>2</sub>. After, the remaining O atoms are attributed to Bi<sub>2</sub>O<sub>3</sub>, and then the left Bi atoms are considered in metallic environment. Details of this calculation are explained in supplementary information. The calculated parts of the three phases are reported in Table 1 for the film, before and after ionic bombardment, and are nicely in agreement with the Bi 4f peak decomposition. Hence, we might consider that in this film, Bi atoms are around 60-67 % in BiO<sub>0.5</sub>F<sub>2</sub>, 28-35% in pure

metallic and 4-5 % in  $\text{Bi}_2\text{O}_3$  environments. Hence, the latter phase seems to be a minor one compared to  $\text{BiO}_{0.5}\text{F}_2$  and Bi.

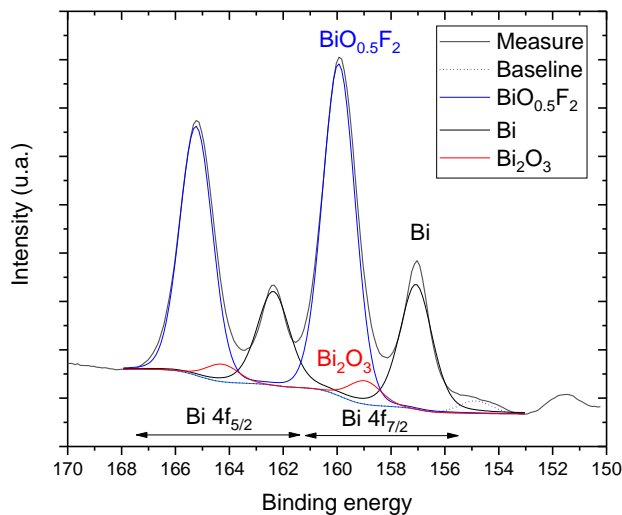


Figure 9: Decomposition of Bi 4f peak for the film deposited at  $R_f = 0.3$  for 20 min after  $\text{Ar}^+$  bombardment.

### 3.4. Photocatalytic properties of thicker films

The degradation of MO in water with films deposited at  $R_f = 0.3$  for 3 and 20 min is illustrated in Figure 10a. The film obtained after 20 min degrades 90 % of MO after only 2 hours of irradiation (compared to only 50% for film deposited during 3 min). Indeed, the crystallization improvement, thanks to higher deposition time, leads to an enhanced photocatalytic activity with a  $k/\text{SA}$  increase from  $3.0$  to  $9.5 \cdot 10^{-3} \text{ min}^{-1} \cdot \text{cm}^{-2}$ . This good results for thicker film may also be explained by its higher roughness and/or a more adapted thickness, reducing the light loss by reflection. To go further, we then check the stability of this best film by cycling experiments (Figure 10b). Its high performance is maintained after 3 cycles (= 9 hours), without major modification observed in its XRD pattern (Figure S2 in supporting information). Hence, this photocatalyst is stable and does not degrade upon irradiation and time.

We might also compare this results to our previous one where we deposited  $\text{Bi}_2\text{O}_3/\text{Bi}$  heterojunction [29]. For the best film, with optimized Bi content, we reached comparable  $k/\text{SA}$  ( $= 8.0 \cdot 10^{-3} \text{ min}^{-1} \cdot \text{cm}^{-2}$ ), which is surprising considering the lower reported  $\text{Bi}_2\text{O}_3$  band gap around 2.6-3.0 eV. From one hand, this can be explained by the fact that the lower bandgap of Bismuth oxide is indirect and so presents a lower absorbance than the direct bandgap of  $\text{BiO}_{0.5}\text{F}_2$ . On the other hand, the fluorination is already reported to create electric local field that reinforce the photogenerated carriers [40] and then limit their recombination. Furthermore, the chemical stability of the oxyfluoride leads to a higher stability of the photocatalyst after 3 cycles than the Bismuth oxide film [29].

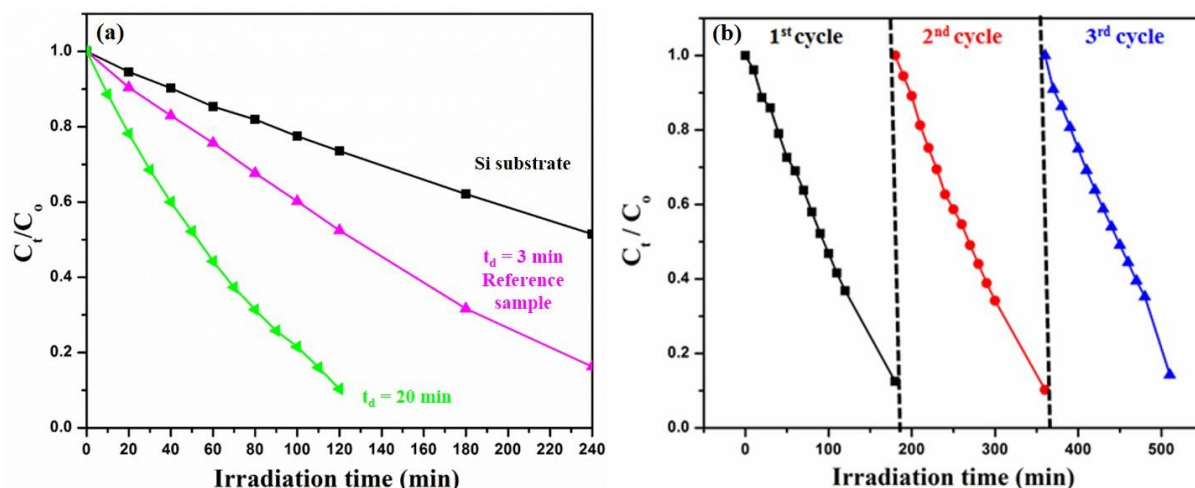


Figure 10: (a) Degradation of MO (Ct/Co) as a function of the irradiation time in the presence of films obtained at  $R_f = 0.3$  for 3 and 20 min of deposition times and (b) cycling curves of photocatalytic degradation for the one deposited during 20 min.

After pollutant photodegradation activity, we investigated the performance of Bismuth oxyfluoride films for  $\text{CO}_2$  photoreduction. Figure 11a presents the electron consumption rate average in photocatalyst mass and in time (on the 20 hours of the test duration) for the  $\text{BiO}_{0.5}\text{F}_2/\text{Bi}$  films (deposited at  $R_f = 0.3$  for 20 min of deposition time). For comparison, we also plotted results for  $\text{Bi}_2\text{O}_3/\text{Bi}$  best film from our previous work and for stoichiometric Bi-based compounds in powder. These latter present relatively low rates compared to films, especially considering that reported values are multiplied by a factor 500. The  $\text{Bi}_2\text{O}_3/\text{Bi}$

heterojunction have interesting rate around 35  $\mu\text{mol/h/g}$ ; while  $\text{BiO}_{0.5}\text{F}_2/\text{Bi}$  system is twice better with a rate around 70  $\mu\text{mol/h/g}$ . The Figure 11a also shows the selectivity of these materials for the different products detected:  $\text{CO}$ ,  $\text{CH}_4$  and  $\text{H}_2$ . It confirms the already observed selectivity of Bi-based photocatalyst for  $\text{CO}$  production.[41] This selectivity is obtained for thin films but also for powders and seems to be reinforced by fluorine presence. It is important to recall that our films present a very low content of carbon. Hence, the detected  $\text{CO}$  comes from  $\text{CO}_2$  reduction and doesn't arise from the oxidation of carbon into the film. The Figure 11b present the production rate ( $r_{\text{av}} \text{ pdt}$ ), averaged on the 20 h of the test duration and normalized by the photocatalyst mass, for the detected reduction products ( $\text{CO}$ ,  $\text{CH}_4$  and  $\text{H}_2$ ). Compared to powder,  $\text{CO}$  gas is identified in 1000 times higher proportion using the thin films. Moreover, taking into account its higher electron consumption rate and its better selectivity for  $\text{CO}$ , the heterojunction of  $\text{BiO}_{0.5}\text{F}_2/\text{Bi}$  developed in this paper is more efficient ( $\approx 25 \text{ mol/h/g}$ ) than the best film  $\text{Bi}_2\text{O}_3/\text{Bi}$  heterojunction ( $\approx 10 \text{ mol/h/g}$ ). Again, this could be explained by a better carrier separation thanks to local electric field into  $\text{BiO}_{0.5}\text{F}_2$  and its direct bandgap. These production rates are comparable to the current state of art [42].

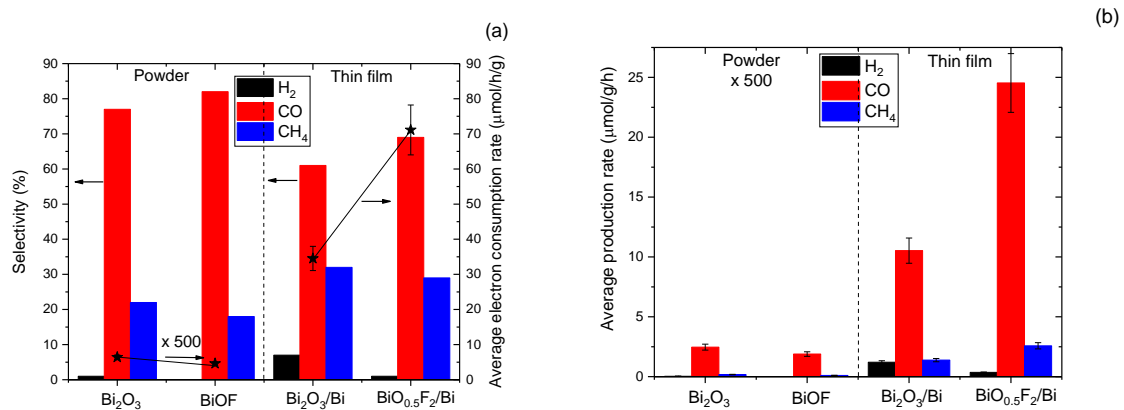


Figure 11: The photocatalytic activity represented by (a) the average electron consumption rate and the selectivity of  $\text{H}_2$ ,  $\text{CO}$ , and  $\text{CH}_4$  products and (b) the average production rate of  $\text{BiO}_{0.5}\text{F}_2/\text{Bi}$  and  $\text{Bi}_2\text{O}_3/\text{Bi}$  film (obtained respectively at  $R_f = 0.3$  and  $\Phi(\text{O}_2) = 1 \text{ sccm}$  [29]), compared to powders.



Finally, for both photocatalytic applications, metallic Bi addition seems to enhance the photocatalytic properties. This can be attributed to different phenomena discussed in literature. First, Bi acts as electron traps, reducing the recombination of the generated  $e^-/h^+$  pairs on the bulk defects of  $\text{BiO}_{0.5}\text{F}_2$  [43], thus enhancing the photocatalytic degradation of MO and photoconversion of  $\text{CO}_2$ . Secondly, metal Bi was shown to act as noble metal nanoparticles (Au and Ag), improving the visible light absorption and activating the photocatalyst [44]. Finally, the surface plasmon polarizes the non-polar reactant molecules and improves the adsorption to the metal surface [43]. Therefore, this heterojunction structure favors the production of  $\text{OH}^\cdot$  radicals at the valence band, which degrade the MO solution, and the photoconversion of  $\text{CO}_2$  at the surface of  $\text{BiO}_{0.5}\text{F}_2$  [45].

#### 4. Conclusions

In this paper, we succeed for the first time to deposit bismuth oxyfluoride thin films by sputtering a Bismuth target in reactive  $\text{Ar}/\text{O}_2/\text{CF}_4$  atmospheres. Moreover, we demonstrate, that the reactive sputtering technique is very versatile, since it allows us to synthesize one-pot heterojunctions of  $\text{BiO}_{0.5}\text{F}_2/\text{Bi}$  with a controlled content of both phases. We also showed that, an increase in the deposition time promotes the part of crystallized phases, leading to improved photocatalytic properties. Finally, the film obtained with  $R_f = 0.3$  and  $t_d = 20$  min exhibits interesting photocatalytic activity in the degradation of MO pollutant in water, stable for at least 9h. It can also be used to selectively convert  $\text{CO}_2$  gas to CO (with a product rate around 25 mmol/h/g and a selectivity of 70%). Yet, this  $\text{BiO}_{0.5}\text{F}_2/\text{Bi}$  heterojunction will be more investigated in the future to understand the exact role of metallic Bismuth in the enhancement of the photocatalytic properties. Moreover, the nanostructuration of such system will be studied to further improve its performance.

## Acknowledgements

The authors acknowledge the support received from the Agence Nationale de la Recherche of the French government through the program “Investissements d’Avenir” (Grant No. 16-IDEX-0001 CAP 20-25).

## References

- [1] A. Fujishima, K. Honda, Electrochemical photolysis of water at a semiconductor electrode, *Nature*. 238 (1972) 37–38.
- [2] X. Jin, L. Ye, H. Xie, G. Chen, Bismuth-rich Bismuth oxyhalides for environmental and energy photocatalysis, *Coord. Chem. Rev.* 349 (2017) 84–101.
- [3] H. Yoshitake, T. Sugihara, T. Tatsumi, Preparation of Wormhole-like Mesoporous TiO<sub>2</sub> with an Extremely Large Surface Area and Stabilization of Its Surface by Chemical Vapor Deposition, *Chem. Mater.* 14 (2002) 1023–1029.
- [4] X. Jia, W. He, X. Zhang, H. Zhao, Z. Li, Y. Feng, Microwave-assisted synthesis of anatase TiO<sub>2</sub> nanorods with mesopores, *Nanotechnology*. 18 (2007) 075602.
- [5] H. Lee, M.Y. Song, J. Jurng, Y.-K. Park, The synthesis and coating process of TiO<sub>2</sub> nanoparticles using CVD process, *Powder Technol.* 214 (2011) 64–68.
- [6] D. Li, M. Carette, A. Granier, J.P. Landesman, A. Goullet, In situ spectroscopic ellipsometry study of TiO<sub>2</sub> films deposited by plasma enhanced chemical vapour deposition, *Appl. Surf. Sci.* 283 (2013) 234–239.
- [7] W. Buraso, V. Lachom, P. Siriya, P. Laokul, Synthesis of TiO<sub>2</sub> nanoparticles via a simple precipitation method and photocatalytic performance, *Mater. Res. Express*. 5 (2018) 115003.
- [8] J. Yang, X. Liu, L. Yang, Y. Wang, Y. Zhang, J. Lang, M. Gao, B. Feng, Effect of annealing temperature on the structure and optical properties of ZnO nanoparticles, *J. Alloys Compd.* 477 (2009) 632–635.
- [9] J. Jie, A. Morita, H. Shirai, Role of oxygen atoms in the growth of magnetron sputter-deposited ZnO films, *J. Appl. Phys.* 108 (2010) 033521.
- [10] X. Chen, Z. Wu, D. Liu, Z. Gao, Preparation of ZnO photocatalyst for the efficient and rapid photocatalytic degradation of azo dyes, *Nanoscale Res. Lett.* 12 (2017) 143.

- [11] J. Li, B. Shen, Z. Hong, B. Lin, B. Gao, Y. Chen, A facile approach to synthesize novel oxygen-doped g-C<sub>3</sub>N<sub>4</sub> with superior visible-light photoreactivity, *Chem. Commun.* 48 (2012) 12017–12019.
- [12] L. Ge, F. Zuo, J. Liu, Q. Ma, C. Wang, D. Sun, L. Bartels, P. Feng, Synthesis and Efficient Visible Light Photocatalytic Hydrogen Evolution of Polymeric g-C<sub>3</sub>N<sub>4</sub> Coupled with CdS Quantum Dots, *J. Phys. Chem. C* 116 (2012) 13708–13714.
- [13] J. Wen, J. Xie, X. Chen, X. Li, A review on g-C<sub>3</sub>N<sub>4</sub>-based photocatalysts, 2nd Int. Symp. Energy Environ. Photocatalytic Mater. 391 (2017) 72–123.
- [14] S. Iyyapushpam, S.T. Nishanthi, D. Pathinettam Padiyan, Synthesis of room temperature bismuth oxide and its photocatalytic activity, *Mater. Lett.* 86 (2012) 25–27.
- [15] M. Ratova, P.J. Kelly, G.T. West, L. Tosheva, M. Edge, Reactive magnetron sputtering deposition of bismuth tungstate onto titania nanoparticles for enhancing visible light photocatalytic activity, *Appl. Surf. Sci.* 392 (2017) 590–597.
- [16] X. Meng, Z. Zhang, Bismuth-based photocatalytic semiconductors: introduction, challenges and possible approaches, *J. Mol. Catal. Chem.* 423 (2016) 533–549.
- [17] H. Cheng, B. Huang, Y. Dai, Engineering BiOX (X = Cl, Br, I) nanostructures for highly efficient photocatalytic applications, *Nanoscale*. 6 (2014) 2009–2026.
- [18] H. Zhang, L. Liu, Z. Zhou, First-principles studies on facet-dependent photocatalytic properties of bismuth oxyhalides (BiOXs), *RSC Adv.* 2 (2012) 9224–9229.
- [19] J. Cheng, L. Frezet, P. Bonnet, C. Wang, Preparation and Photocatalytic Properties of a Hierarchical BiOCl/BiOF Composite Photocatalyst, *Catal. Lett.* (2018) 1–8.
- [20] M. Yang, Q. Yang, J. Zhong, J. Li, S. Huang, X. Li, PVA-assisted hydrothermal preparation of BiOF with remarkably enhanced photocatalytic performance, *Mater. Lett.* 201 (2017) 35–38.
- [21] S. Zou, F. Teng, C. Chang, Z. Liu, S. Wang, Controllable synthesis of uniform BiOF nanosheets and their improved photocatalytic activity by an exposed high-energy (002) facet and internal electric field, *RSC Adv.* 5 (2015) 88936–88942.
- [22] M. Yang, Q. Yang, J. Zhong, S. Huang, J. Li, J. Song, C. Burda, Enhanced photocatalytic performance of Ag<sub>2</sub>O/BiOF composite photocatalysts originating from efficient interfacial charge separation, *Appl. Surf. Sci.* 416 (2017) 666–671.
- [23] T. Jiang, J. Li, Y. Gao, L. Li, T. Lu, L. Pan, BiOBr/BiOF composites for efficient degradation of rhodamine B and nitrobenzene under visible light irradiation, *J. Colloid Interface Sci.* 490 (2017) 812–818.
- [24] W. Gu, G. Zhang, F. Teng, Y. Teng, Z. Zhao, W. Fan, Effect of F/O atomic ratio on photocatalytic activity of Bi<sub>x</sub>O<sub>y</sub>F<sub>z</sub>, *Chem. Phys. Lett.* 659 (2016) 221–224.

- [25] M. Ren, F. Teng, Y. Yang, Y. Zhai, W. Gu, Z. Liu, Z. Liu, Y. Teng, Influence of O/F ratio on oxygen defect and photochemical properties of BixOyFz, *Mater. Des.* 131 (2017) 402–409.
- [26] J.C. Medina, M. Bizarro, C.L. Gomez, O. Depablos-Rivera, R. Mirabal-Rojas, B.M. Monroy, A. Fonseca-Garcia, J. Perez-Alvarez, S.E. Rodil, Sputtered bismuth oxide thin films as a potential photocatalytic material, *Nov. Nanomater. Photocatal. Photochem. Photobiol.* 266 (2016) 144–152.
- [27] A. Dolgov, D. Lopaev, C.J. Lee, E. Zoethout, V. Medvedev, O. Yakushev, F. Bijkerk, Characterization of carbon contamination under ion and hot atom bombardment in a tin-plasma extreme ultraviolet light source, *Appl. Surf. Sci.* 353 (2015) 708–713.
- [28] M. Bervas, B. Yakshinskiy, L. Klein, G. Amatucci, Soft-chemistry synthesis and characterization of bismuth oxyfluorides and ammonium bismuth fluorides, *J. Am. Ceram. Soc.* 89 (2006) 645–651.
- [29] S. Ibrahim, P. Bonnet, M. Sarakha, C. Caperaa, G. Monier, A. Bousquet, Tailoring the structural and optical properties of bismuth oxide films deposited by reactive magnetron sputtering for photocatalytic application, *Mater. Chem. Phys.* 243 (2020) 122580.
- [30] Agnès Granier, Gael Borvon, Angélique Bousquet, Antoine Goullet, Christiane Leteinturier, Arie van der Lee, Mechanisms Involved in the Conversion of ppHMDSO Films into SiO<sub>2</sub>-Like by Oxygen Plasma Treatment, *Plasma Processes and Polymers* 3 (2006) 100–109.
- [31] H. Fan, G. Wang, L. Hu, Infrared, Raman and XPS spectroscopic studies of Bi<sub>2</sub>O<sub>3</sub>–B<sub>2</sub>O<sub>3</sub>–Ga<sub>2</sub>O<sub>3</sub> glasses, *Solid State Sci.* 11 (2009) 2065–2070.
- [32] J. Yang, T. Xie, C. Liu, L. Xu, Facile Fabrication of Dumbbell-Like  $\beta$ -Bi<sub>2</sub>O<sub>3</sub>/Graphene Nanocomposites and Their Highly Efficient Photocatalytic Activity, *Materials*. 11 (2018) 1359.
- [33] Y. Li, Y. Wang, K. Wang, F. Gomado, G. Wang, L. Tang, X. Rong, The effect of N-ethyl-N-hydroxyethyl perfluorooctanoamide on wettability alteration of shale reservoir, *Sci. Rep.* 8 (2018) 1–9.
- [34] W. Hu, P. Shan, T. Sun, H. Liu, J. Zhang, X. Liu, Y. Kong, J. Xu, Preparation, nonlinear optical properties, and theoretical analysis of the non-centrosymmetric bismuth oxyfluoride, Bi<sub>7</sub>F<sub>11</sub>O<sub>5</sub>, *J. Alloys Compd.* 658 (2016) 788–794.
- [35] F. He, Z. He, J. Xie, Y. Li, IR and raman spectra properties of Bi<sub>2</sub>O<sub>3</sub>-ZnO-B<sub>2</sub>O<sub>3</sub>-BaO quaternary glass system, *Am. J. Anal. Chem.* 5 (2014) 1142.
- [36] J. Cheng, L. Frezet, P. Bonnet, C. Wang, Preparation and photocatalytic properties of a hierarchical BiOCl/ BiOF composite photocatalyst, *Catalysis Letters*, 2012, 1-8
- [37] W.L. Huang, Q. Zhu, Electronic structures of relaxed BiOX (X=F, Cl, Br, I) photocatalysts, *Comput. Mater. Sci.* 43 (2008) 1101–1108.

- [38] Y. Huang, S. Kang, Y. Yang, H. Qin, Z. Ni, S. Yang, X. Li, Facile synthesis of Bi/Bi<sub>2</sub>WO<sub>6</sub> nanocomposite with enhanced photocatalytic activity under visible light, *Appl. Catal. B Environ.* 196 (2016) 89–99.
- [39] A.J. Gmitter, A. Halajko, P.J. Sideris, S.G. Greenbaum, G.G. Amatucci, Subsurface diffusion of oxide electrolyte decomposition products in metal fluoride nanocomposite electrodes, *Electrochimica Acta.* 88 (2013) 735–744.
- [40] H.-Y. Jiang, J. Liu, K. Cheng, W. Sun, J. Lin, Enhanced Visible Light Photocatalysis of Bi<sub>2</sub>O<sub>3</sub> upon Fluorination, *J. Phys. Chem. C.* 117 (2013) 20029–20036.
- [41] G. Ren, X. Zhang, C. Zhang, et al., Synergetic effect of Bi<sub>2</sub>WO<sub>6</sub> micro-spheres and activated carbon mm-spheres for enhancing photoreduction activity of CO<sub>2</sub> to CO, *Materials Letters*, 264, 2020, 127201.
- [42] S. Sorcar, S. Yoriya, H. Lee, C.A. Grimes, S.P. Feng, A review of recent progress in gas phase CO<sub>2</sub> reduction and suggestions on future advancement, *Mater. Today Chem.*, 16, 2020, 100264.
- [43] X. Zhang, Y.L. Chen, R.-S. Liu, D.P. Tsai, Plasmonic photocatalysis, *Rep. Prog. Phys.* 76 (2013) 046401.
- [44] P. Wang, B. Huang, Y. Dai, M.-H. Whangbo, Plasmonic photocatalysts: harvesting visible light with noble metal nanoparticles, *Phys. Chem. Chem. Phys.* 14 (2012) 9813–9825.
- [45] W. Li, D. Li, J. Xian, W. Chen, Y. Hu, Y. Shao, X. Fu, Specific analyses of the active species on Zn<sub>0.28</sub>Cd<sub>0.72</sub>S and TiO<sub>2</sub> photocatalysts in the degradation of methyl orange, *J. Phys. Chem. C.* 114 (2010) 21482–21492.

## Supporting Information

**Figure S1.**

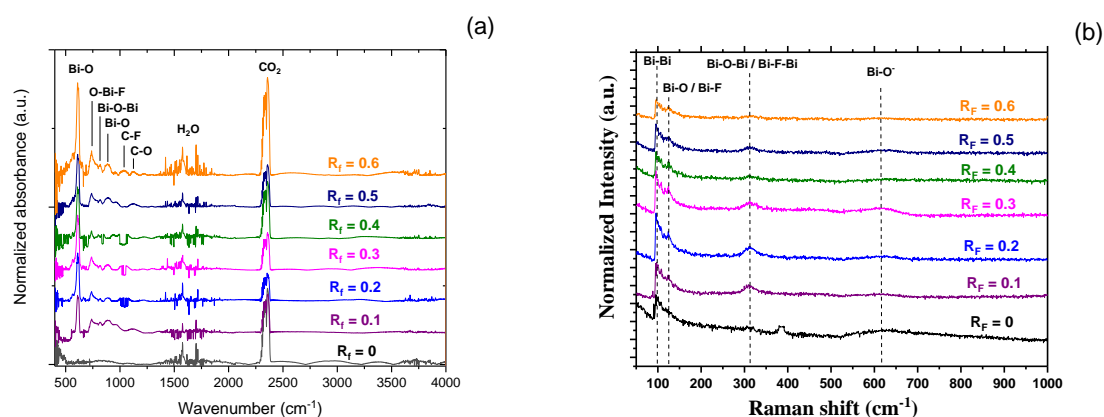


Figure S1: (a) Infrared absorption spectra and (b) Raman spectra of bismuth oxyfluoride films deposited for  $R_f$  ranging from 0 to 0.6.

**XPS peaks position, width and area, before and after Ar<sup>+</sup> bombardment, for the film deposited at  $R_f = 0.3$  for 20 min.**

| Elements     | Environment  | Before        |            |         | After Ar <sup>+</sup> bombardment |            |         |
|--------------|--|---------------|------------|---------|-----------------------------------|------------|---------|
|              |  | Position (eV) | Width (eV) | Area    | Position (eV)                     | Width (eV) | Area    |
| <b>Bi 4f</b> | <b>Bi<sup>0</sup></b>                                    | 157.2         | 1.40       | 47 903  | 157.1                             | 1.42       | 154 467 |
|              | <b>Bi<sup>3+</sup> in Bi<sub>2</sub>O<sub>3</sub></b>    | 159.0         | 1.40       | 19 846  | 159.0                             | 1.42       | 25 640  |
|              | <b>Bi<sup>3+</sup> in BiO<sub>0.5</sub>F<sub>2</sub></b> | 160.0         | 1.40       | 400 653 | 160.0                             | 1.42       | 375 259 |
| <b>O 1s</b>  | <b>O-Bi in BiO<sub>0.5</sub>F<sub>2</sub></b>            | 530.5         | 1.28       | 19 314  | 530.6                             | 1.38       | 20 628  |
|              | <b>O=C</b>   | 531.1         | 2.23       | 6 407   | 531.5                             | 1.63       | 829     |
|              | <b>C-O-C</b>   | 532.3         | 2.23       | 5 459   | 532.2                             | 1.63       | 1 744   |
| <b>F 1s</b>  | <b>F in BiO<sub>0.5</sub>F<sub>2</sub></b>               | 684.2         | 1.6        | 92 588  | 684.3                             | 1.59       | 102 699 |
| <b>C 1s</b>  | <b>C-C</b>   | 285.3         | 1.48       | 4 673   | 285.1                             | 1.7        | 1 366   |
|              | <b>C-O</b>   | 286.9         | 1.48       | 882     |                                   |            |         |
|              | <b>C-F</b>   | 288.9         | 1.48       | 788     |                                   |            |         |

## Details of parts of various Bi environment from XPS analysis

We calculate the contributions of the three different Bi environment ( $\text{BiO}_{0.5}\text{F}_2$ ,  $\text{Bi}_2\text{O}_3$  and Bi) from the elemental composition, considering the peaks attributed to a Bi-based compound, e.g. peaks in bold in the previous table. Hence, we do not take into account peaks originating from dust (such as  $\text{O}=\text{C}$  or  $\text{C}-\text{O}-\text{C}$  contributions which are clearly differentiated from O-Bi contributions in O 1s spectrum); but we are not influenced by peak fitting of Bi 4f (considering its whole area). We obtained for film after the  $\text{Ar}^+$  bombardment: **39.9 % of Bi**, 13.6 % of O and 46.5 % of F. From this elemental composition, we considered that all F atoms are from  $\text{BiO}_{0.5}\text{F}_2$ . Hence, **23.3 % of Bi**, 11.6 % of O and 46.5 % of F belong to  $\text{BiO}_{0.5}\text{F}_2$  compound. After, the remaining O atoms (= 2 %) are attributed to  $\text{Bi}_2\text{O}_3$ . Indeed, **1.3 % of Bi** and 2 % of O belong to  $\text{Bi}_2\text{O}_3$  compound. The left Bi atoms (**15.3 %**) are considered in metallic environment. Finally, the Bi atoms are for 58.4 % (= 23.3 % compared to 39.9 total % of Bi atoms) in  $\text{BiO}_{0.5}\text{F}_2$ , 3.3 % in  $\text{Bi}_2\text{O}_3$  and 38.3 % in metallic environments.

**Figure S2.**

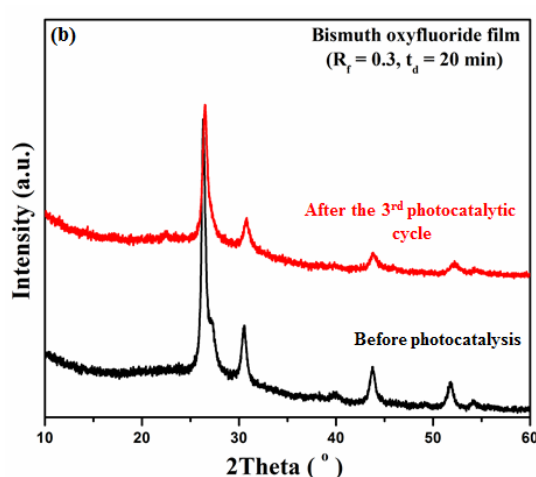


Figure S2: XRD pattern for the film deposited for  $R_f = 0.3$  for 20 min, before and after 3 cycles of 2 hours of photodegradation experiment.